

Implementing Inkjet-Printed Transparent Conductive Electrodes in Solution-Processed Organic Electronics

Felix Hermerschmidt,* Stelios A. Choulis, and Emil J. W. List-Kratochvil*

Through the use of solution-based materials, the field of printed organic electronics has not only made new devices accessible, but also allows the process of manufacture to move toward a high throughput industrial scale. However, while solution-based active layer materials in these systems have been studied quite intensely, the printed electrodes and specifically the transparent conductive anode have only relatively recently been investigated. In this progress report, the use of metal nanoparticles within printed organic electronic devices is highlighted, specifically their use as replacement of the commonly used indium tin oxide transparent conductive electrode within organic photovoltaics (OPVs) and organic light emitting diodes (OLEDs). A cross fertilization between the applications is expected since an OPV device is essentially an inversely operated OLED. This report aims to highlight the use of inkjet-printed nanoparticles as cost-effective electrodes for printed optoelectronic applications and discusses methods to improve the conductive and interfacial properties. Finally, in an outlook, the use of these types of metal nanoparticle inks to manipulate light management properties, such as outcoupling, in the device is investigated.

leading to modern day OLED applications, which include the displays used in smart-phones, tablets and e-readers, in foldable touch screens and in some curved lighting devices.^[3–7]

The other main branch of organic electronics, organic photovoltaics, has not been quite as commercially successful, even though new efficiency records are being set all the time.^[8] However, brought on through the latest advent of perovskites,^[9–11] this new branch of hybrid organic photovoltaic device promises to give a newfound resurgence to the field of organic/hybrid photovoltaics.^[12]

One of the major advantages of these types of electronic devices is that they can be manufactured using a solution-based processing route, i.e., from solutions or inks or even pastes that contain the active material dissolved in a suitable solvent system. These solutions can then be deposited using standard lab-based techniques such as spin coating, but also using sophisticated, technology-relevant

processing systems such as inkjet-printing or roll-coating.^[13,14] Organic field effect transistors (OFETs), highly efficient organic photovoltaics (OPVs) and high-performance OLEDs, have been fabricated using inkjet printing, thereby underlining the versatility of this printing method.^[15–20]

1. Introduction—Solution Processed Organic Electronics

The field of organic electronics has gained substantial momentum in the past 20 to 30 years. The discovery of electroluminescent polymers in the early 90s^[1] has led to commercialization of the organic light emitting diode (OLED),^[2]

1.1. A Brief Overview of Device Functionality

However, especially in high efficiency OLED structures, vacuum-processed stacks of materials are usually utilized, with at least one organic semiconductor layer sandwiched between a transparent conductive oxide (TCO)—which serves as the transparent conductive anode—and usually a vacuum-deposited low work function metal—which serves as the cathode. The organic active layers are either deposited by vacuum sublimation of small molecules or in a wet chemical process from a solution of conjugated polymers.

In a traditional multilayer OLED, the emissive layer (EML) is sandwiched between a hole-transporting layer (HTL) and an electron-transporting layer (ETL). At flat-band conditions, i.e., no external bias, energy barriers between the HTL and EML as well as the ETL and EML can be identified (see **Figure 1**). When an external bias is applied, the energy barriers can be overcome and the injection of charge carriers can take place, leading to

Dr. F. Hermerschmidt, Prof. E. J. W. List-Kratochvil
Humboldt-Universität zu Berlin
Institut für Physik
Institut für Chemie
IRIS Adlershof
Brook-Taylor-Straße 6, 12489 Berlin, Germany
E-mail: felix.hermerschmidt@hu-berlin.de;
emil.list-kratochvil@hu-berlin.de

Prof. E. J. W. List-Kratochvil
Helmholtz-Zentrum
Berlin für Materialien und Energie GmbH
Brook-Taylor-Straße 6, 12489 Berlin, Germany
Prof. S. A. Choulis
Cyprus University of Technology
Department of Mechanical Engineering and Materials Science
and Engineering
45 Kitiou Kyprianou Street, 3041 Limassol, Cyprus

DOI: 10.1002/admt.201800474

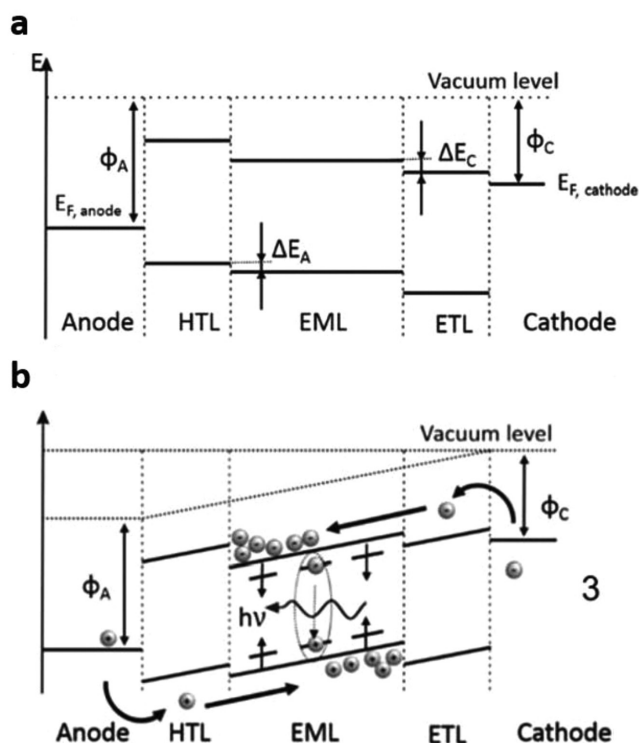


Figure 1. In flat-band conditions a) electrons and holes encounter an energy barrier (ΔE_A and ΔE_C), while under an applied external bias b), this energy barrier can be overcome and holes and electrons can recombine in the emitter material (EML). Adapted with permission.^[21] Copyright 2014, The Royal Society of Chemistry.

photons ultimately generated by the recombination of the injected charge carriers within the active layer.^[22–24] Using this architecture, the injection of holes and electrons is facilitated, leakage of the “wrong” carrier toward the electrode is prevented and any recombination/quenching processes occurring at the electrodes are avoided.^[25–27]

An OPV device, on the other hand, is essentially an inversely operated light-emitting diode (see **Figure 2**). In OPVs, the incident photons ultimately lead to free charge carriers, which contribute to an external current. As opposed to silicon-based solar cells,^[28] in OPV bulk heterojunction systems consisting of a conjugated polymer donor/fullerene acceptor organic semiconductor blend, the photoexcitation of an electron occurs from the donor HOMO into its LUMO after light absorption to form an exciton.^[29–32] The excitons diffuse within the donor phase and dissociate upon encountering an interface with the fullerene acceptor.^[33] Charge transfer then results in an intermolecular charge-transfer (CT) state, whereby the electron and hole are located on the acceptor and donor, respectively.^[34,35] However, as the charges may still be bound to one another via Coulomb forces, an electric field is needed to separate them into free charges.^[36] Finally, the free charges (electrons and holes) have to be transported toward the carrier selective electrodes along their respective domain. Those excitons that do not reach the bulk heterojunction interface recombine and therefore do not contribute to the photocurrent.^[37]



Felix Hermerschmidt received his Ph.D. in materials science and engineering from Cyprus University of Technology, focusing on inkjet-printed active layers and electrodes in organic solar cells and organic light emitting diodes under the supervision of Prof. Stelios A. Choulis. Before that, having obtained his B.Sc. in chemistry at

Freie Universität Berlin, he completed an MRes in green chemistry at Imperial College London, focusing on morphology control in solution-processed solar cell active layers under the supervision of Profs. Natalie Stingelin and James R. Durrant. He is currently a postdoctoral researcher in Prof. Emil List-Kratochvil's Hybrid Devices group at Humboldt-Universität zu Berlin with expertise in the formulation, processing and characterization of functional materials in hybrid optoelectronic devices as well as in printed electronics.



Stelios A. Choulis is Professor of Material Science and Engineering at the Cyprus University of Technology (2008–present). He was the Organic Photovoltaic Device group leader of Konarka Technologies (2006–2008) and research and development (R&D) engineer of the Osram Opto-Semiconductors Inc.

Organic Light Emitting Diode R&D team (2004–2006). During his Ph.D. and first postdoc research associate (PDRA) position at the Advanced Technology Institute (1999–2002, University of Surrey), he investigated the optical properties of quantum electronic materials and optoelectronic devices. In 2002, he joined the center of electronic materials and devices (Imperial College London, UK) as PDRA and worked on the transport and recombination dynamics properties of molecular semiconductor materials and devices (2002–2004). His current research interest focuses on the development of functional materials and novel electrodes for solution processed optoelectronic applications.

1.2. Some Examples of Solution-Processed Devices

Since the functional layers in solution-processed OLEDs and OPVs are deposited one on top of another, it is imperative that one deposited layer does not chemically or physically interact with the previously deposited layer underneath it. In the case of solution-based processing this is not trivial. For example, water-based hole-transporting layers such as poly(3,4-ethylenedioxythi



Emil List-Kratochvil graduated in technical physics (1998) and received a doctoral degree in experimental solid-state physics (2000) from Graz University of Technology, where he also went on to complete his habilitation in solid-state physics (2003) to become Associate Professor (2004). Between 2006 and 2015 he

was appointed as a Scientific Managing Director of the NTC Weiz GmbH. Since 2015 he is a full Professor for Hybrid Devices in a joint appointment in the departments of physics and chemistry of Humboldt-Universität zu Berlin. He is an expert in (printed) semiconductor devices and structure to property relationships in organic and hybrid semiconductors. With his team, he is currently working on electronic and optoelectronic components (based on hybrid material systems and organic or hybrid semiconductors), additive resource-efficient deposition techniques and in situ nanostructuring and synthesis methods. Since 2018, he is also a leader of the joint research group Generative Production Processes for Hybrid Components at Helmholtz-Zentrum Berlin.

ophene):poly(styrenesulfonate) (PEDOT:PSS) have a strong influence on some active material classes, such as perovskites.^[39,40] In order to tackle the issue of dissolution of already applied layers during the fabrication of well-defined multilayer structures in a solution-based process, Auer et al. looked at several mechanisms and methods to enable the fabrication of efficient multilayer (double and triple active layer) OLED structures.^[21]

One such example utilizes crosslinking to thermally stabilize a hole-transporting compound via annealing at 200 °C, after which it is completely insoluble to organic solvents. By spin-coating a blue emissive compound on top, highly efficient fluorescent blue emitting two-layer OLEDs were produced.^[41] The top electrode consisted of thermally evaporated Cs₂CO₃/Al, while the transparent anode was ITO covered with PEDOT:PSS.

The same thermal stabilization approach can be utilized to sandwich an emissive layer in between a crosslinked and insolubilized hole-transporting layer, while depositing a polar soluble, i.e., orthogonal, electron-transporting layer on top.^[42,43] OLEDs based on such an architecture showed an increase in the rate of exciton generation by facilitating charge carrier confinement in the emissive layer, thereby improving recombination and proving the effectiveness of this multilayer approach.

These examples highlight the importance of understanding the interface behavior between the individual components of a multilayer optoelectronic device. However, all devices discussed are based on ITO/PEDOT as the transparent anode material system. We will now discuss in detail the effect of replacing the ITO in both OPV and OLED systems with inkjet-printed structures and its effect on the interfacial properties and resulting device performance.

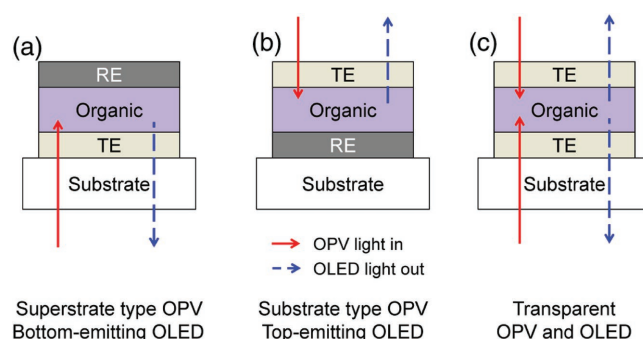


Figure 2. The common device architectures employed for OPVs and OLEDs underline the reciprocal nature of their functionality. a) Light transfers into the superstrate-type OPV and out of the bottom-emitting OLED through the transparent substrate and transparent electrode (TE), while being reflected off the reflective electrode (RE), b) light transfers into the substrate type OPV and out of the top-emitting OLED through the top transparent electrode; and c) light transfers in and out of the transparent OPV and OLED through both the bottom and top transparent electrodes. Reproduced with permission.^[38] Copyright 2014, SPIE Digital Library.

2. The Printed Transparent Conductive Electrode in Organic Electronics

2.1. Inkjet Printing

Inkjet printing is an additive, direct write, non-contact technique, compatible with printing manufacturing and requiring no masks or lithographic pre patterning of substrates. It incorporates drop-on-demand (DoD) technology, which enables ink droplets to be deposited exactly where required on the desired substrate, minimizing material loss as a consequence.^[44] Inkjet-printing can also be transferred to a roll-to-roll (R2R) process,^[45,46] thereby accessing both a productivity of up to 6 m² min⁻¹ and also small feature sizes (30–50 μm line/10 μm space) and a wide variety of shapes.^[47–50] Inkjet printing has been utilized in order to fabricate every component of an organic optoelectronic device, including the active layer materials and the metal top and transparent bottom electrodes.^[16,17,51,52] However, only very few devices have claimed to be wholly inkjet-printed,^[53–55] paving the way for fully solution-processed devices to become more widespread.

One of the key differences to other solution-based deposition techniques such as spin coating and doctor blading is that solution deposition occurs automatically through a print-head with a particular drop volume and nozzle number (see **Figure 3**). Solution viscosity of the inks is a crucial parameter, as the piezoelectric mechanism must be able to eject the solution sufficiently out of the nozzles. Since the temperature of the cartridge can also be adjusted, this viscosity can be altered (in most cases decreased by increasing the temperature) to provide more desired properties.

The second key difference to other deposition techniques is that deposition occurs in a line-by-line fashion (much like an inkjet printer in the home) and therefore each printed line must merge with the previous and next printed line in order to form a homogenous and morphologically smooth film on the substrate.^[52]

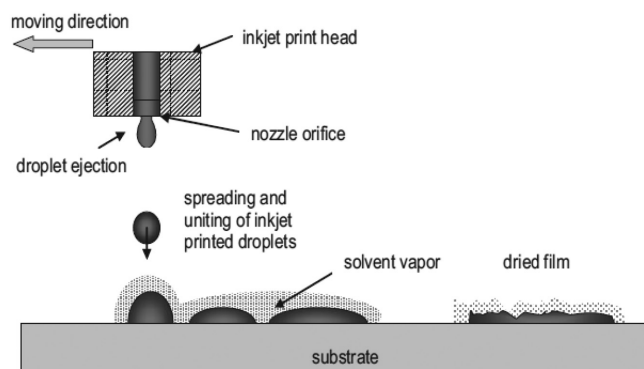


Figure 3. During the inkjet printing process, the printhead moves across the substrate, ejecting single droplets, which then merge and form a dried film after solvent evaporation. Reproduced with permission.^[56] Copyright 2007, Wiley VCH.

Overall, it is possible to control the temperature of the print-head/cartridge and the temperature of the substrate. The range of temperature control of the substrate usually does not extend beyond 60–80 °C, since above this temperature undesired evaporation of solvent can occur at the printhead nozzles, leading to clogging. Furthermore, the drop spacing, the distance of the printhead to the substrate and the amounts of nozzles used for deposition (each nozzle can be individually addressed) can be adjusted. It is also possible to adjust each nozzle's individual firing voltage to eject the droplets, as well as the overall waveform, which provides details on the amount of pressure used to eject each droplet.

2.2. Transparent Conductive Electrodes and Printed Metal Grid Design

As shown above, most high efficiency organic electronic device architectures are based upon ITO as the transparent electrode. ITO, however, has an inherent limit in its range of applications due to its brittle nature, cost and its low-throughput method of production.^[57,58] With a sheet resistance of $\approx 5 \Omega \text{ sq}^{-1}$ it is suitable for small area devices, but at larger scale, where higher conductivity is essential, this becomes a limiting factor.^[59] It is therefore desirable to replace ITO with other materials, which is especially important when targeting flexible OLED lighting or smart packaging applications. Several other types of transparent electrodes have been investigated, including high conductivity polymers such as PEDOT:PSS,^[60–62] graphene-based and other novel material electrodes,^[63,64] carbon nanotubes,^[65] Ag and Cu nanowires,^[66,67] Cu mesh,^[68] and a variety of thermally evaporated metal grids.^[69–71] Transparent metal oxides, used together with a metal (grid) contact, can also be evaporated or sputtered, while some metal oxides such as ZnO, Al-doped ZnO, and WO₃ are routinely being deposited by solution-processing, including inkjet-printing.^[53,72–74]

Solution-processed metal nanoparticles in the form of printable inks have also been investigated,^[55,75] but most approaches utilize photolithography and require several (subtractive rather than additive) processing steps.^[76–79] The implementation of a metal nanoparticle-based anode is usually made by creating a

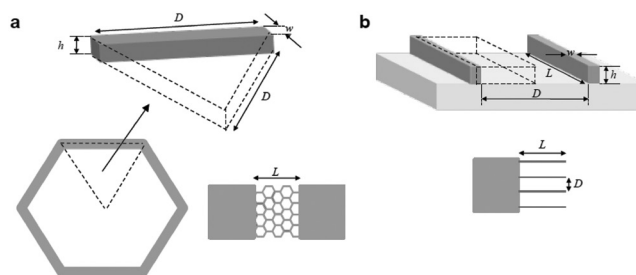


Figure 4. When implementing a) a hexagonal grid or b) a straight line architecture as the printed conducting electrode, the spacing L between busbars, spacing D between lines and grid as well as the width w and height h of the structures themselves need to be taken into consideration. Reproduced with permission.^[80] 2014, I. Burgués-Ceballos.

printed structure in the form of a grid or mesh and then overcoating this with a transparent conducting material, such as PEDOT:PSS. This serves two purposes: first, it “spreads” the area of conductivity from the direct metallic areas of the grid itself to cover also the areas where no metal structure is present, second, it helps to planarize the printed structure, by overcoating small defect sites and thereby enabling a smooth contact area with the following organic layer.

The two geometries shown in **Figure 4** have gained particular attention: a straight line layout and a honeycomb layout, which have been explored in great detail by Burgués-Ceballos.^[80] The honeycomb design provides an advantage versus the straight-line geometry: any possible breaks in the line that have occurred during the printing or drying process do not influence the overall current collection efficiency as significantly, since charges have the possibility to be rerouted through alternative paths along the honeycomb grid. However, a straight-line geometry is simpler, easier to print and more easily adjusted regarding size of the grid itself and the techniques used to prepare the grids.

Burgués-Ceballos estimated the losses sustained by a Ag grid/PEDOT:PSS electrode due to shadowing and resistive effects by adapting a numerical model,^[81] and using experimentally obtained input parameters.^[80] Some typical OPV performance parameters were also considered in the model based on reference devices.^[82]

In the case of the linear geometry, the minimum losses of $\pm 3\%$ were situated in a wider pitch range of between 720 and 2480 μm (see **Figure 5**), while the corresponding range of minimum losses was much lower in the honeycomb structure (180–1110 μm). However, the losses due to shadowing and sheet resistance contributed more markedly at the extremes in the honeycomb structure.

Moreover, as the insets of **Figure 5** show, by simply changing the line width the linear geometry allows a wider range of optimum pitch to be accessed. This is important for two reasons: first, by widening the lines, a lower line density can be employed in a linear geometry, leading to a reduced use of metal ink; secondly this lower line density can improve the success of the imprinting transfer described later in the text.^[80] On the other hand, employing a honeycomb structure can reduce the total losses below 2% when very thin lines are deposited, which is in stark contrast to the minimum 7.6% achievable by using the linear geometry.

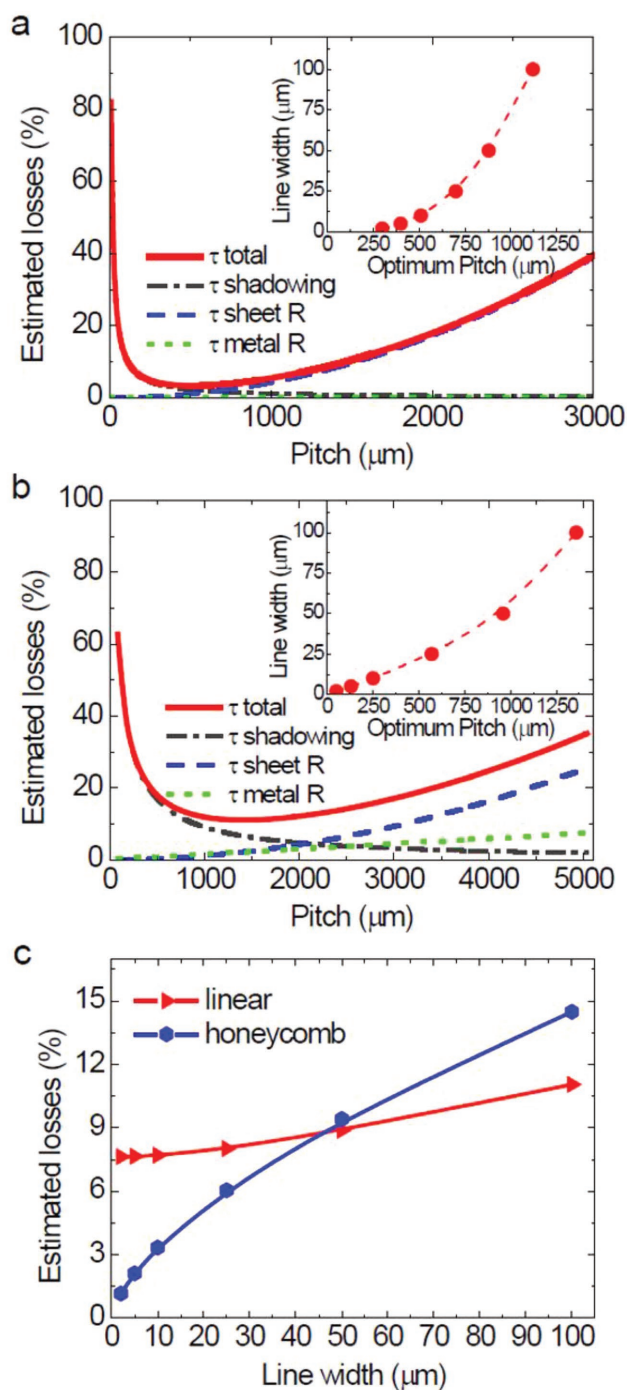


Figure 5. The calculated contribution of the shadowing and resistive losses as a function of pitch show a greater difference at the pitch extremes for a) the honeycomb grid architecture than for b) the lines. At the same time, overall losses are smaller over a wider range of line widths in the case of the linear architecture than for honeycomb, allowing c) a greater processing window. Reproduced with permission.^[80] Copyright 2014, I. Burgués-Ceballos.

Overall, two distinct regimes were differentiated: The honeycomb geometry yields lower total losses when employing line widths below 50 μm , while above that width the linear geometry shows lower total losses. For very thin lines and the low

losses attributed to those, the use of the honeycomb structure may be preferential.^[80]

2.3. Metal Nanoparticle Inks

The discussed grids need to be deposited from an ink and the majority of ink formulations can be divided into roughly two categories: inks containing capped metal nanoparticles and metal organic decomposition inks.^[83] Generally, the inks contain a low metal content and (organic) stabilizers to prevent nozzle clogging during printing and to comply with printhead restrictions concerning viscosity and surface tension. Some inks are available with up to 70 wt% metal loading, but these require control of any sedimentation process that may occur.

During a sintering process which commonly follows the ink deposition, the deposited ink is transformed into a uniform and conductive film suitable for use in electronic structures. In the case of capped metal nanoparticles the capping is removed, while for the metal organic decomposition the ink precursors decompose to form the final film. A wide variety of sintering treatments (laser, flashlamp, microwave, thermal, plasma, electrical, chemical) have been reported for metal particle inks,^[83–89] and all of these methods have varying advantages and disadvantages concerning throughput and geometry dependency.

The specific nature of each sintering treatment (e.g., photonic vs chemical) has an effect on the duration of treatment and its suitability. For example, laser sintering is slow (≈ 10 – 15 min per A4 sheet) compared to flash light sintering (in seconds) but has the benefit that different structures can be treated in an optimized manner.^[84] This is due to photonic sintering being geometry dependent, meaning that different line widths and film thicknesses possess different optimal parameters regarding time and intensity of the treatment.

Photonic sintering additionally requires substrates with a defined and suitable thermal conductivity, since the control of the dissipation of a high amount of photogenerated heat in a short period of time during the sintering process is critical.^[90] If the thermal conductivity is too high, it can prevent enough heat from sintering the ink due to rapid dissipation. However, flexible substrates with low thermal conductivity can be subject to rupture or delamination of the formed structures. For silver sintering, due to the metal's high oxidation resistance and good electrical conduction even in oxidized states,^[91] simple thermal processes can be applied making the required sintering step to form uniform films of merged nanoparticles less demanding.

3. Previous Work on Printed Transparent Conducting Electrode Grids

Past approaches to printable conductive metal structures to provide a grid-based transparent anode have focused mainly on silver due to the abovementioned advantages. An early proceedings paper reported organic light-emitting diodes containing silver nanoparticle grids as an ITO replacement.^[92] However, while those early results showed how applicable the proposed maskless deposition method was for large area devices, no

specific information was given regarding the efficiency of the OLEDs based on the Ag grid line/PEDOT:PSS electrodes versus ITO. By combining the metal grids with a highly conducting PEDOT:PSS as the transparent anode electrode, hole-injection into the emitting material was facilitated. OLEDs with an active area of several cm² were produced and scaled to approximately 150 cm², including on flexible PEN substrates. The grid lines were 120 nm in height and were able to be sufficiently overcoated with a thick layer of PEDOT:PSS.

3.1. Overcoating—Control of the Printed Metal Grid Line Height

Indeed this direct overcoating has been reported in a variety of publications that have dealt with inkjet-printed and sintered silver grids based on nanoparticle inks for use in organic electronic devices (see Table 1). The height and width of most grid lines was approximately in the range of 100–400 nm and 50–200 μm, respectively. When utilized in solar cell applications, this height regime can yield an equivalent device performance to ITO-based devices. This is achieved by covering the grids with a layer of PEDOT:PSS, which fully coats the grid lines in order to prevent shunts (see Figure 6).

However, this same height of the combined grid line/PEDOT:PSS electrode can usually not simply be transferred to OLED applications. This is because arguably in OLEDs the accuracy of the PEDOT:PSS layer thickness plays a much greater role than in solar cells. Not only does the layer need to be transparent and conductive enough, but the properties of hole-injection need to be optimal across a greater voltage range as well as being balanced to the device's electron-injecting characteristics.

The electrode therefore usually needs to be entirely reexamined in order to establish the required characteristics to

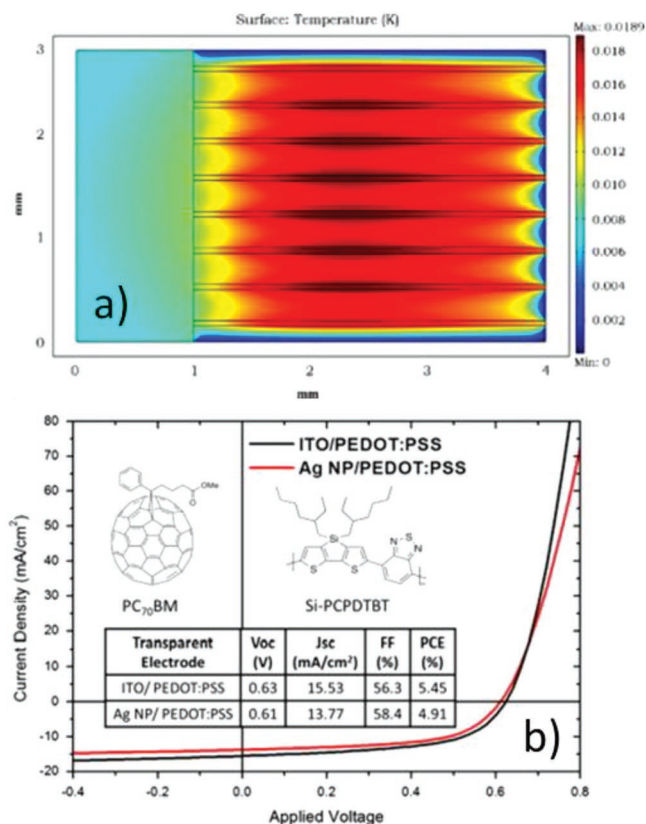


Figure 6. a) A homogeneous temperature distribution is achieved within the transparent electrode used in OPV devices based on an eight-line Ag grid coated with PEDOT:PSS, b) both ITO-free and ITO-based OPVs containing eight-line Ag grid/PEDOT:PSS electrodes show similar device performance parameters. Adapted with permission.^[17] Copyright 2014, Elsevier.

Table 1. The tabular overview compares inkjet-printed transparent conducting electrodes based on Ag ink, which have been subjected to a simple overcoat of the subsequent layer. Unless indicated, the printed electrode functions as the bottom transparent anode in the device. For comparison regarding line dimensions, photolithography is included in one instance.

References	Deposition method	Device	Material	Grid type	Width/space	Height	Sheet resistance	Transmittance
Harkema SPIE 2009 ^[92]	Inkjet	OLED	Ag ink (Cabot AG-IJ-G-100-S1)	Lines	200 μm/–	120 nm	1 Ω sq ^{−1}	–
Galagan SEMSC 2012 ^[93]	Inkjet	OPV	Ag ink (Suntronic U5603)	Hexagonal	215 μm/5 mm	250–400 nm	5–12 Ω sq ^{−1}	–
Galagan AEM 2012 ^[47]	Inkjet	OPV	Ag ink (Suntronic U5603)	Lines	300 μm/≥1 mm	500 nm	1–20 Ω sq ^{−1}	–
Neophytou APL 2012 ^[16]	Inkjet	OPV	Ag ink (Suntronic U5603)	Lines	50 μm/700 μm	200 nm	–	>90%
Galagan SEMSC 2014 (top electrode) ^[94]	Inkjet	OPV	Ag ink (Suntronic U5603)	Lines	100 μm/2 mm	200 nm	–	>80%
Neophytou SEMSC 2014 ^[17]	Inkjet	OPV	Ag ink (Suntronic U5603)	Lines	50 μm/–	200 nm	8.5 Ω sq ^{−1}	>90%
Sam OE 2014 ^[76]	Photolithography	OLED	Evaporated Ag	Hexagonal	2 μm/60 μm 3 μm/10 μm	10 nm 40 nm	200 Ω sq ^{−1} 7 Ω sq ^{−1}	>94%
EGgenhuisen JAMC 2015 ^[54]	Inkjet	OPV	Ag ink (Suntronic U5603)	Lines	–	–	7 Ω sq ^{−1}	–
Patil OE 2015 (top and bottom electrodes) ^[95]	Inkjet	OPV	Ag ink (Suntronic U5603)	Lines	250 μm/2 mm	250–300 nm	0.63 Ω sq ^{−1}	>85%
Hermerschmidt FPE 2016 ^[15]	Inkjet	OLED	Ag ink (Suntronic U5603)	Lines	90 μm/200 μm	70–80 nm	0.2 Ω sq ^{−1}	>80%
Polino AMI 2016 (top electrode) ^[96]	Inkjet	OPV	Ag ink (Suntronic U5603)	Lines	100 μm/2 mm	400 nm	0.27 Ω sq ^{−1}	–
Kinner APL 2017 ^[49]	Inkjet	OLED	Ag ink (Cabot CCI 300)	Hexagonal	350 μm/3–8 mm	400–800 nm	<5 Ω sq ^{−1}	>75%

achieve a similar device performance to ITO-based OLEDs. One aim is to reduce the height of the grid electrode in order to cover it with a minimum amount of PEDOT:PSS, so as to remain comparable to the common reference PEDOT:PSS thickness of ≈ 50 nm on ITO. One approach has therefore been to print grid lines on top of glass substrates previously treated with UV-O₃, which results in an increase of surface free energy and better wetting of the nanoparticle ink (see Figure 7).

As a result of this treatment, the height and width of the resulting grid line was 70–80 nm and ≈ 90 μm , respectively, therefore allowing the grid to be coated with a thinner layer of PEDOT:PSS. However, the treatment time must be carefully controlled, as too long UV-O₃ treatment yields even thinner but wider lines, due to greater spreading of the ink. If the lines are too wide, transmittance is compromised.

As crucially as confirming the optimum grid line parameters, the optimum PEDOT:PSS thickness with which to coat these grid lines needed to be examined. Due to the low line height of ≈ 70 –80 nm, a thin PEDOT:PSS layer was targeted to cover these lines. As shown in Figure 7, PEDOT:PSS thicknesses between 85 and 205 nm were investigated on both 8- and 10-line grid architectures. When using thicker PEDOT:PSS films (125–175 nm), higher maximum luminance values were achieved, indicating that the combination of silver grid and PEDOT:PSS provides the best hole-injecting properties, while maintaining enough transmittance and fully covering the grids.

For all PEDOT:PSS thicknesses investigated, the 10-line grid architecture produces higher luminance and luminous efficiency (LE), with a PEDOT:PSS layer of 150 nm thickness providing the most favorable grid/PEDOT:PSS combination. This indicates improved charge injection from the Ag grid into the PEDOT:PSS layer, which would result in a more favorable charge distribution across the entire anode.

An additional effect of the improved injection properties is the lower voltage at which peak LE occurred in the device based on the 10-line grid, when compared to the ITO-based devices, e. g. at 4 V, LE is 1.25 cd A^{-1} for the 10-line grid compared to 1.18 cd A^{-1} for ITO. Overall, at low-to-medium brightness, the performance parameters showed similar device efficiencies, while at higher luminance values, the ITO-based devices performed slightly better (data not shown here).

In order to understand these performance differences between grid-based and ITO-based OLEDs, the complete devices were analyzed using photocurrent mapping,^[97] which provides information on the current distribution within the device. Local defects that are visualized using this technique may be an indication of diminished performance.

As can be seen in Figure 8, the ITO-based OLED yielded a current distribution with no visible interruptions overall and an almost uniform current of $\approx 0.7 \mu\text{A}$ produced throughout the entire device. The Ag grid-based OLED yielded lower currents, which showed slight variations (0.55 – $0.65 \mu\text{A}$), but the current distribution was also rather uniform, indicating a well-functioning device overall. The obtained results prove that the implemented Ag grid/PEDOT:PSS structure is a viable alternative to ITO to produce OLEDs with similar performance parameters.^[15]

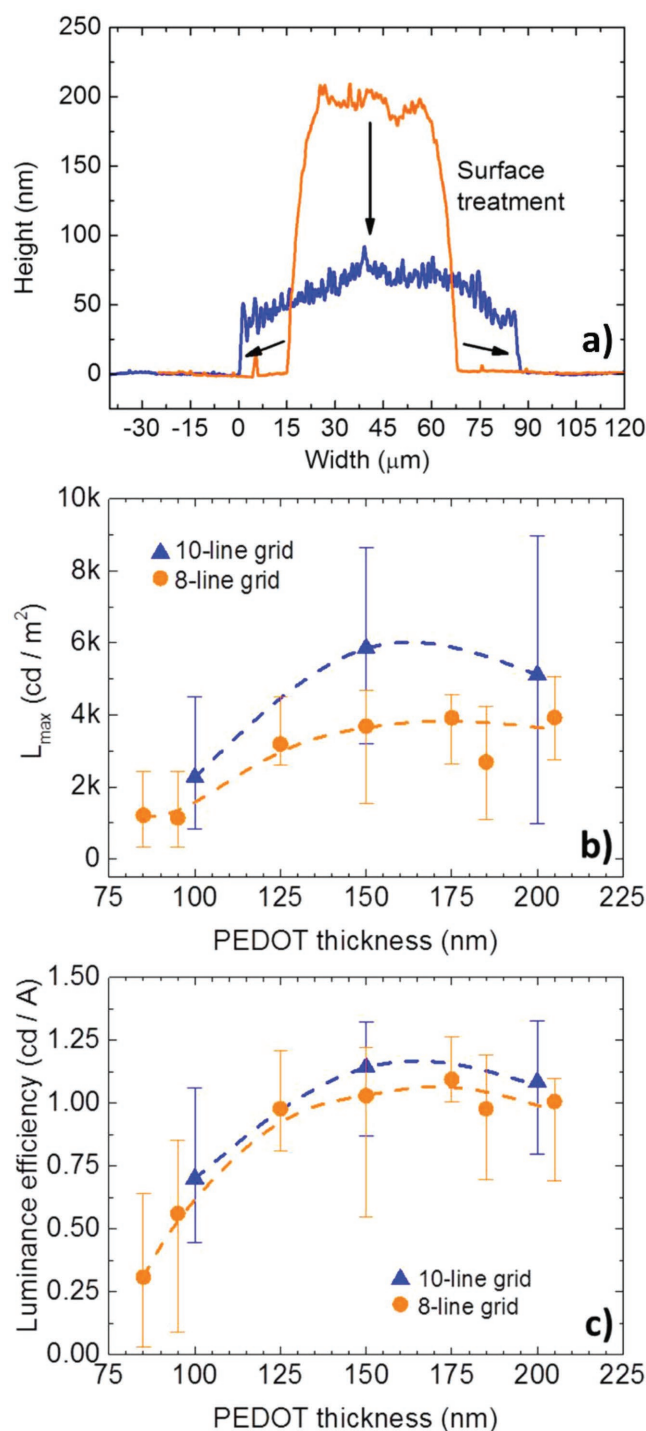


Figure 7. a) Following UV-O₃ surface treatment, the printed line height is reduced dramatically, b,c) the grid containing 10 printed lines achieves superior luminance and luminous efficiency performance for all PEDOT thicknesses examined. Adapted with permission.^[15] Copyright 2016, IOP Publishing.

3.2. Embedding the Inkjet-Printed Grid

As mentioned above, in order to improve OLED performance based on these types of grid architectures further, an extremely

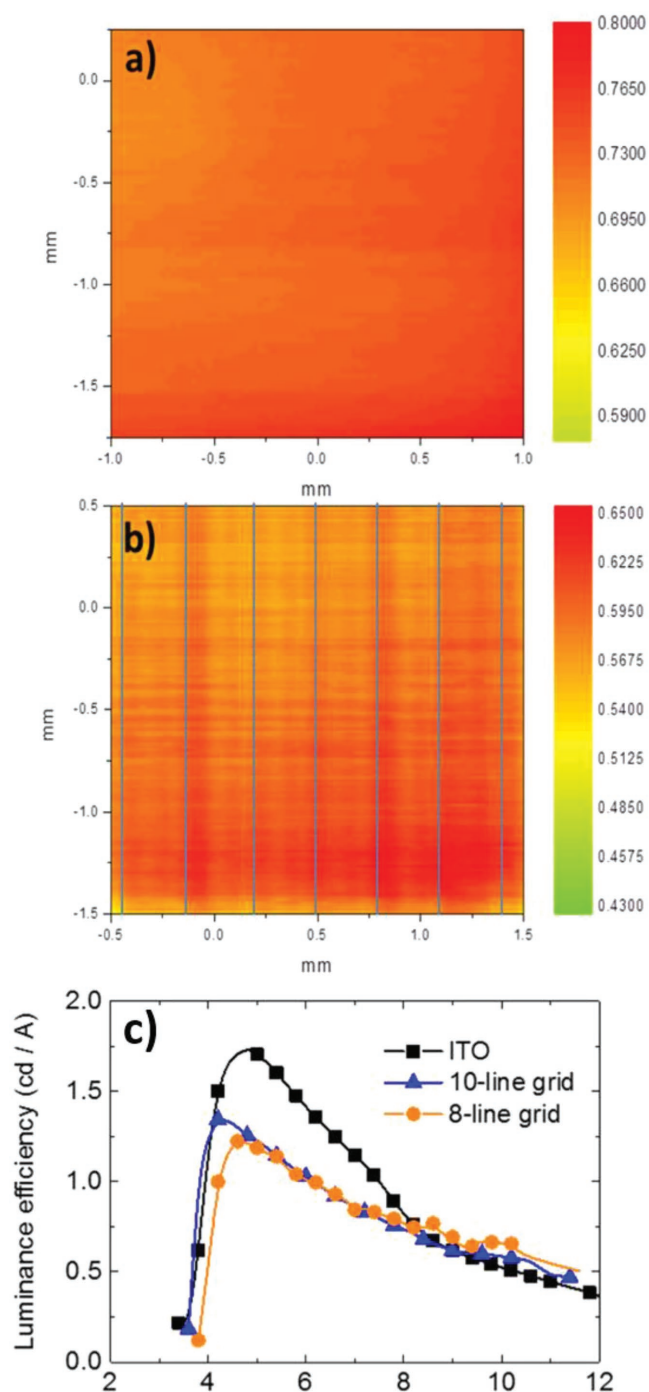


Figure 8. The photocurrent map of a 4 mm² OLED based on a) ITO shows slightly more homogeneous current distribution than b) the 10-line silver nanoparticle grid. Note that the nominal grid position is superimposed on the image. c) Comparable luminous efficiency can be seen for OLEDs based on ITO and ITO-free silver grid electrodes. Adapted with permission.^[15] Copyright 2016, IOP Publishing.

flat and smooth electrode surface must be achieved. This will yield more homogeneous electric fields, improved injection of charge carriers, and result in more homogenous light emission. A useful method to achieve this is to embed the electrodes

within a resin. This kind of embedding process for inkjet-printed electrodes was first proposed and developed for use in OPVs.^[75] By building on this approach, Kinner et al. reported the first OLEDs based on embedded and non-embedded inkjet-printed metal-grid/PEDOT:PSS electrodes.^[49]

In this case, the Ag grid was inkjet-printed in a honeycomb layout in order to utilize the advantages described in Section 2.2 above. The honeycomb structure provides a balance between reducing the surface coverage (and thereby reducing shadowing) as well as providing a sufficient and homogeneously distributed number of conductive pathways, even in the case of any local line breakages after printing. The embedding was carried out using a commercially available resin (Ormocer). With this approach any defect or roughness in the printed structure can be overcome.

In fact, the inkjet-printed grid lines were not only embedded within the resin but also transferred from the sacrificial to the final substrate by being flipped over, resulting in upside-down lines after printing (see Figure 9). The entire electrode configuration was thus planarized and provides a completely flat surface compared to non-embedded lines, which may have small imperfections. Additionally, the transfer process allows the ink to be printed on virtually any substrate before being transferred to virtually any other substrate.

The OLED stack with inkjet-printed non-embedded and embedded Ag lines is schematically shown in Figure 10. Before embedding, any imperfections such as spikes in the surface topography can cause shorts or parasitic currents through the layers. After embedding, the grid lines have been flattened and planarized by the nanoimprinting transfer and a thin layer of PEDOT:PSS can be used to overcoat any remaining surface imperfections, thereby further reducing the risk of shorts and leakage currents through the complete device.

Additionally, a thinner PEDOT:PSS films provides greater transparency and the optical transmittance was evaluated by honeycombs with different spacing diameters. Since these type of printed grid electrodes have some areas with 100% transmittance where there is no grid line and 0% transmittance where there are grid lines, these measurements should be interpreted as the average transmittance at each grid spacing. The final inkjet-printed Ag grids (8 mm spacing diameter, 350 μ m line width) showed comparable transmittance in the relevant optical range to ITO (data not shown here) but yielded device efficiencies significantly higher than OLEDs based on ITO. The embedding process reduces prevalent leakage currents and, more importantly, significantly improves light outcoupling, an effect which will be discussed in detail in Section 5 below.

The achieved luminescence characteristics of the described OLEDs are shown in Figure 10. The reference ITO-based OLED yielded a maximum luminance of 20 000 cd m⁻². While the OLED based on the non-embedded 3 mm grid/PEDOT:PSS electrode yielded a maximum luminance of 9000 cd m⁻², OLEDs based on the embedded 3 and 5 mm grid/PEDOT:PSS electrodes yielded maximum luminance values of 40 000 and 42 000 cd m⁻², respectively. Finally, the OLED based on the 8 mm grid/PEDOT:PSS electrode showed a maximum luminance of 20 000 cd m⁻². Normalized electroluminescence spectra resulting from OLEDs based on the 8 mm grid/PEDOT:PSS electrode are shown in the inset of Figure 10.

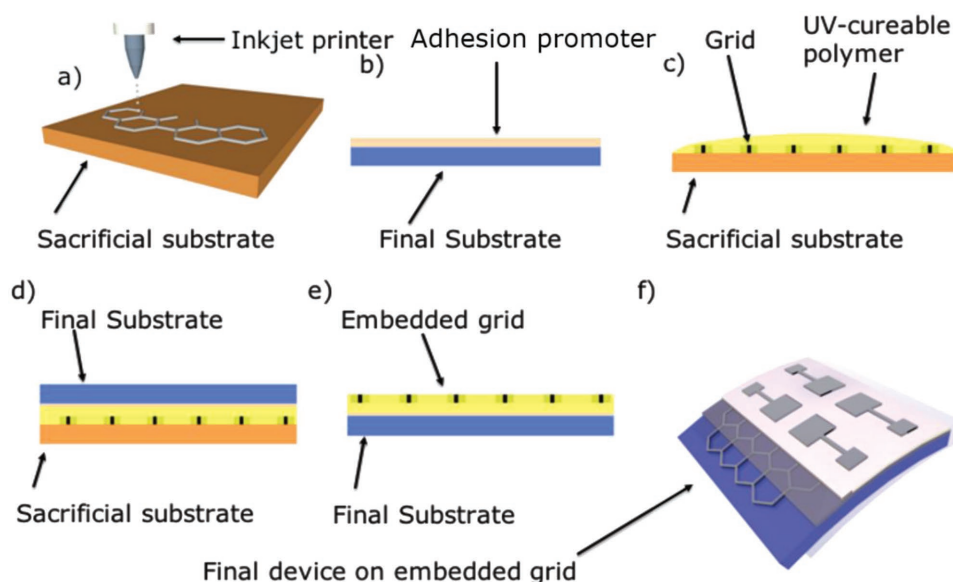


Figure 9. The reverse nanoimprinting transfer results in embedded Ag grid electrodes. a) The desired electrode pattern is printed onto a sacrificial substrate, b) an adhesion promoter (Ormoprime08) is coated on the final substrate, c) a UV curable resin is coated onto the sacrificial substrate/Ag grid structure, d) the two substrates are brought together and exposed to pressure and UV light, e) removal of the sacrificial substrate yields the desired Ag grid structure embedded within the resin, f) the final device can be processed on top of this embedded grid structure. Process based on ref. [75].

These confirm the stability of the emission of the light-emitting polymer at two different luminance values and are similar to the spectra obtained for OLEDs based on the reference ITO/PEDOT:PSS electrode (data not shown here).

In addition to the luminance values, Figure 10 also shows the current densities obtained from the measured OLEDs. The most prominent feature is shown by the black arrow, which indicates the difference in leakage current of almost four orders of magnitude between the devices based on the non-embedded grid/PEDOT:PSS electrodes and the other electrode types. Importantly however, after the grid electrodes are embedded, the resulting OLEDs show leakage currents 400 times lower than those based on non-embedded grids. While this is still one order of magnitude higher than the ITO-based reference (which overall show the lowest leakage currents) this was largely expected since ITO is a much flatter electrode system than even the embedded grids and hence provides the lowest possibility of shorts through the device. Of the grid-based devices, the OLED containing 8 mm embedded grid/PEDOT:PSS electrodes showed the lowest values in terms of leakage current and was the highest performing device overall.^[49]

4. Transferring from Ag to Cu Metal Nanoparticle Inks

When looking at the findings detailed in the above sections, the results obtained by the various groups worldwide have shown that using silver nanoparticle ink in a current collecting or transporting grid has been thoroughly investigated and understood. Several reports have provided evidence of improved grid functionality when moving from simple straight-line to more complex geometry. This is undoubtedly as a result of an improved interface between the grid itself and the next layer

processed on top of it. Through the continuous improvement of this interface and the understanding of specific interface effects such as those that can be used to couple light out of the device more efficiently (see Section 5) even greater device performance can be achieved in printed organic optoelectronic devices employing Ag grids.

However, while Ag has many of the benefits discussed in the above sections, its disadvantages are its high costs and its susceptibility to electromigration.^[98] Overcoming these disadvantages is the reason for targeting Cu as the basis to forming low cost inks to use in current collecting grids, with its lower raw material price and high bulk conductivity (Cu: $5.96 \times 10^5 \text{ S cm}^{-1}$, Ag: $6.30 \times 10^5 \text{ S cm}^{-1}$, at 20°C).^[99,100] As with Ag, the developed inks must be suitable for large area processing methods such as R2R and additive deposition methods like inkjet printing.

However, Cu suffers from high chemical reactivity and due to the poor electrical conductivity of oxidized Cu films, it is important to prevent oxidation during the sintering of the Cu ink. One such method is by utilizing formic acid vapor,^[101] or by applying a reducing agent directly into an inkjet mixture during or just before the printing process.^[102–105] The printed circuit board and semiconductor industry already implements formic acid in its manufacturing processes.^[106,107]

4.1. Organic Photovoltaics Based on Cu Metal Grids

Georgiou et al. presented the first optoelectronic devices based on inkjet-printed Cu grids as a replacement for ITO.^[18] The solution-processed Cu nanoparticles produced high quality Cu grids with good adhesion to the substrate and the required conductivity. ITO-free OPVs based on these inkjet-printed Cu grids in combination with PEDOT:PSS were produced using the

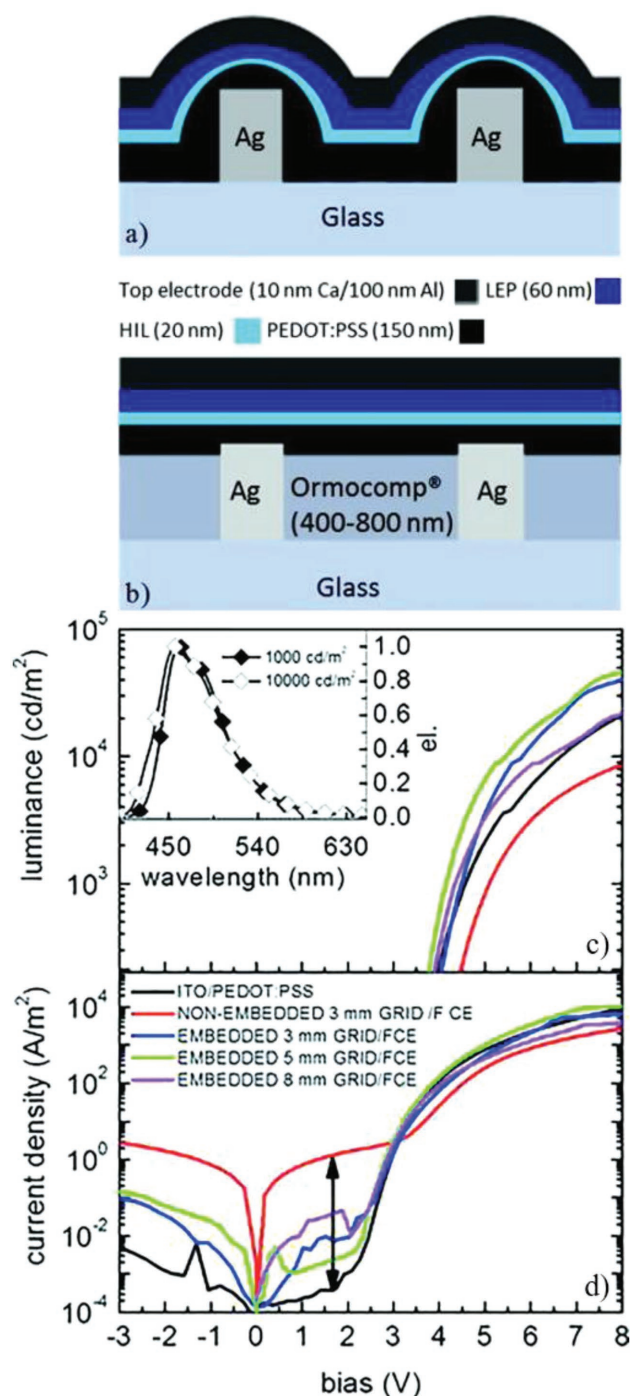


Figure 10. a,b) Following the embedding process, the grid lines can not only be coated with a much thinner layer of PEDOT:PSS, but the risk of shunts due to penetrating metal structure is vastly reduced. c) The resulting device performance shows maximum luminance values between 9000 and 42 000 cd m^{-2} , while embedding reduces d) the leakage current by orders of magnitude. Adapted with permission.^[49] Copyright 2017, American Institute of Physics.

organic polymer/fullerene active layer blend of poly[2,6-(4,4-bis-(2-ethylhexyl)dithieno[3,2-b:2',3'-d]silole)-alt-4,7-(2,1,3-benzothiadiazole)]/[6,6]-phenyl C_{71} butyric acid methyl ester

(Si-PCPDTBT)/PC[70]BM) as active layer material. A power conversion efficiency (PCE) of 3.35% was achieved, while ITO-based OPVs reached a PCE of 4.92%.

The lower PCE was primarily due to oxidation of the deposited Cu grid and the reduced conductivity arising from the required annealing step of PEDOT:PSS performed in ambient conditions. Initial trials on embedding the inkjet-printed Cu grids using the same reverse nanoimprinting transfer procedure described above produced Si-PCPDTBT/PC[70]BM OPVs with a PCE of 2.56%.

As before in the case of the development process for the Ag grid-based electrode, the entirety of the electrode needed to be re-examined. This resulted in a variety of Cu grid electrodes being fabricated and tested—with a pitch of 0.6 mm (4 lines), 0.43 mm (6 lines), and 0.33 mm (8 lines). Implementing these different grids into complete OPV devices yielded an improvement of the fill factor (FF) in those OPVs containing a greater number of Cu grid lines. The short-circuit current (J_{sc}) also increased with an increasing number of lines, however, for the highest number of lines the losses due to shadowing became more dominant.

As a result, the optimum balance between carrier collection and shadowing losses was achieved for OPVs employing a six-line grid, giving a J_{sc} of 11.39 mA cm^{-2} and FF of 50.72%. The reference OPV device based on ITO showed a higher J_{sc} of 14.12 mA cm^{-2} and FF of 57.84%, and the majority of these losses in J_{sc} were due to shadowing effects of the Cu grid design and the lower transmittance resulting from needing a thicker PEDOT:PSS layer to overcoat the grid lines.

In addition to the performance parameters obtained under illuminated conditions, dark current density/voltage (J/V) curves were recorded. These provide further information on the potential loss regimes in device performance (see Figure 11). The data show a much higher series resistance (R_s) of the Cu grid-based OPVs than those based on ITO, owing to the low current density at forward bias. R_s is an indicator for the resistance the current experiences in the vertical direction between the layers and interfaces of the OPV device, meaning that a large factor influencing R_s is the conductivity of the electrode,^[108,109] since all other stack layers are identical. One possible reason for a lower conductivity of the inkjet-printed Cu grids could be due to breakages along the printed lines.

At the same time, the Cu grid-based OPVs show a higher leakage current (i.e., a lower parallel resistance, R_p) than ITO-based OPVs, which was similarly observed by Kinner et al.^[49] This can be an indicator for unfavorable morphology of the printed Cu grid lines, i.e., some spikes or other imperfections may not have been fully overcoated by PEDOT:PSS, while the ITO again would have a flat and homogeneous morphology. As a result of both the increased R_s and the reduced R_p values, Cu grid-based OPVs show lower overall FF than the reference ITO-based OPVs.

As for the Ag grid-based devices, photocurrent mapping measurements were carried out (Figure 11),^[97] in order to determine possible defects in photocurrent distribution across the Cu grid structures within the complete OPV devices. The current distribution was efficient and homogeneous for the four-line and six-line Cu grid configuration, but lower and less homogeneous for the eight-line Cu grid, which was confirmed by the J_{sc} values. Overall, therefore, the six-line grid

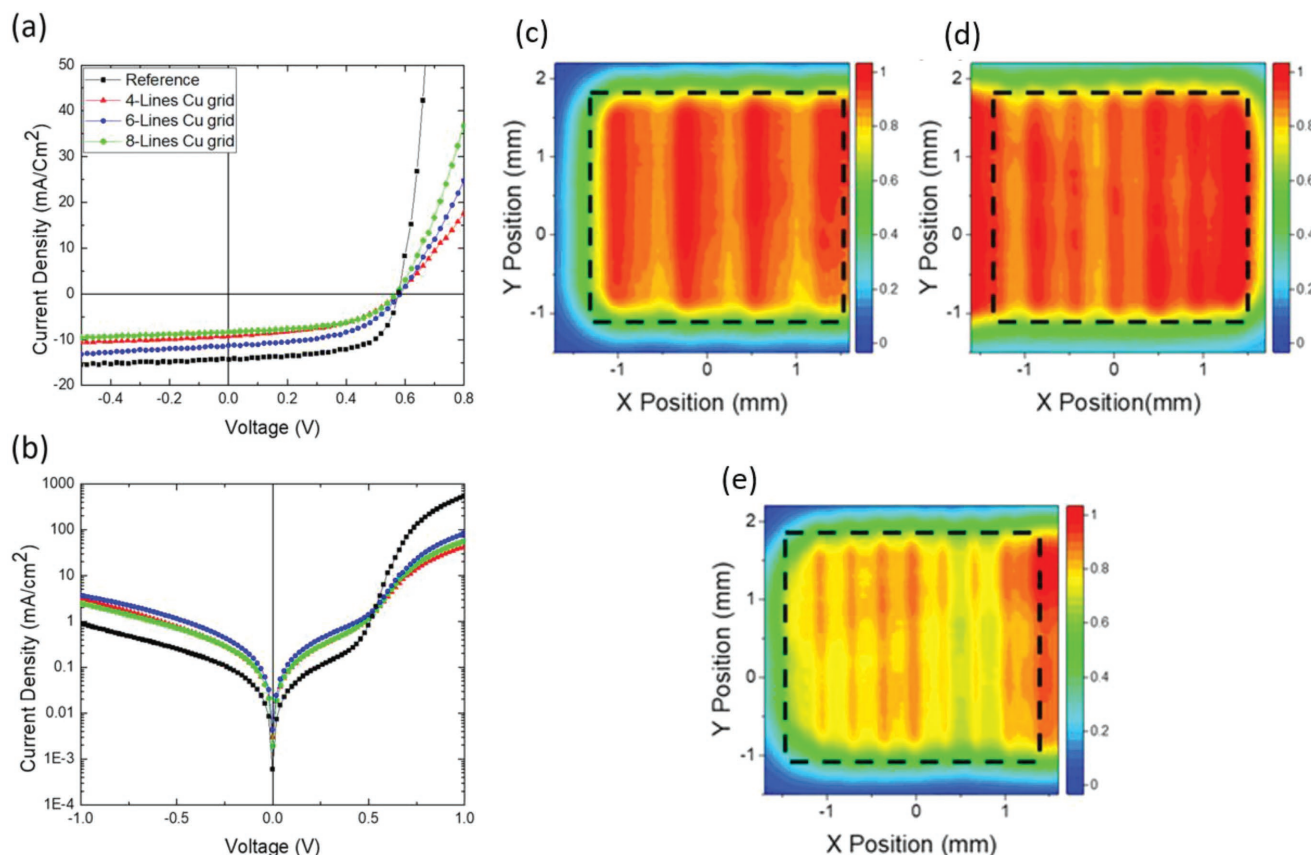


Figure 11. The J/V curves (a,b) show significantly higher series resistance for the ITO-free OPVs, resulting from losses in electrode conductivity. The photocurrent maps (c,d,e) confirm the most homogenous current distribution using the six-line grid architecture (d), when compared to the four-line and eight-line grid (c,e). Adapted with permission.^[18] Copyright 2018, Wiley VCH.

architecture yielded the optimum OPV performance in this system.^[18]

4.2. Overcoming the Oxidation Limitation of Cu by Sintering

As described above, Cu requires a postdeposition treatment process to overcome the limitations from oxidation. The OPV devices described in the previous section implement laser-sintered Cu nanoparticle grids, which can reach limitations regarding throughput and material substrate compatibility. These limitations can be overcome by a method of postdeposition treatment and sintering of Cu ink using formic acid in a procedure that is compatible with the use of low-cost flexible substrates with low glass transition temperatures.^[110] The additive process is chemically facile, scalable, uses minimal material and is compatible with R2R processing, thus industrially feasible, yielding structures that have excellent adhesion and stability under manual bending tests to within 2% tensile strain.

The resulting Cu films fabricated at the truly low temperature of 130 °C showed a conductivity of up to 16% bulk Cu ($9.7 \times 10^4 \text{ S cm}^{-1}$) together with ISO 0 adhesion on glass as well as on the flexible substrate polyethylene terephthalate (PET). When employing sintering temperatures above 130 °C the bulk Cu conductivity increased to a remarkable 25%

($1.6 \times 10^5 \text{ S cm}^{-1}$) for 150 °C and reached 31% ($1.8 \times 10^5 \text{ S cm}^{-1}$) for 230 °C.

Importantly, the 16% bulk Cu conductivity is fully suited for use as conductive features in electronic devices and is comparable to the conductivity obtained from photonically sintered Cu ink-based structures, while the achieved conductivity values for sintering temperatures at and above 150 °C were the highest reported values for conductive, thin (<500 nm) Cu films.

The introduced process for sintering of Cu-based nanoparticle inks was as follows: After the deposition and subsequent drying at 80 °C (see Figure 12), homogenous non-conducting films were obtained. X-ray photoemission spectroscopy (XPS) studies (Figure 12b) revealed a C1s peak resulting from the organic protective ligand of the nanoparticles as well as the solvent surroundings. At the same time, the Cu2p signal shows an abundant presence of oxidized (non-conductive) Cu(II) species.

The XPS data in Figure 12 also display the depth profile evolution of the signal achieved via sputtering. The topmost curves refer to the bare sample surface; the middle curves to a depth of $\approx 5 \text{ nm}$, and the bottommost curves to a depth of $\approx 20 \text{ nm}$. Through the worsening signal-to-noise ratio, the depth profile indicates consistently that the C1s signal decreases while that of the Cu2p increases. Particularly, the peak related to Cu(II) fully disappears, indicating the presence of metallic Cu.

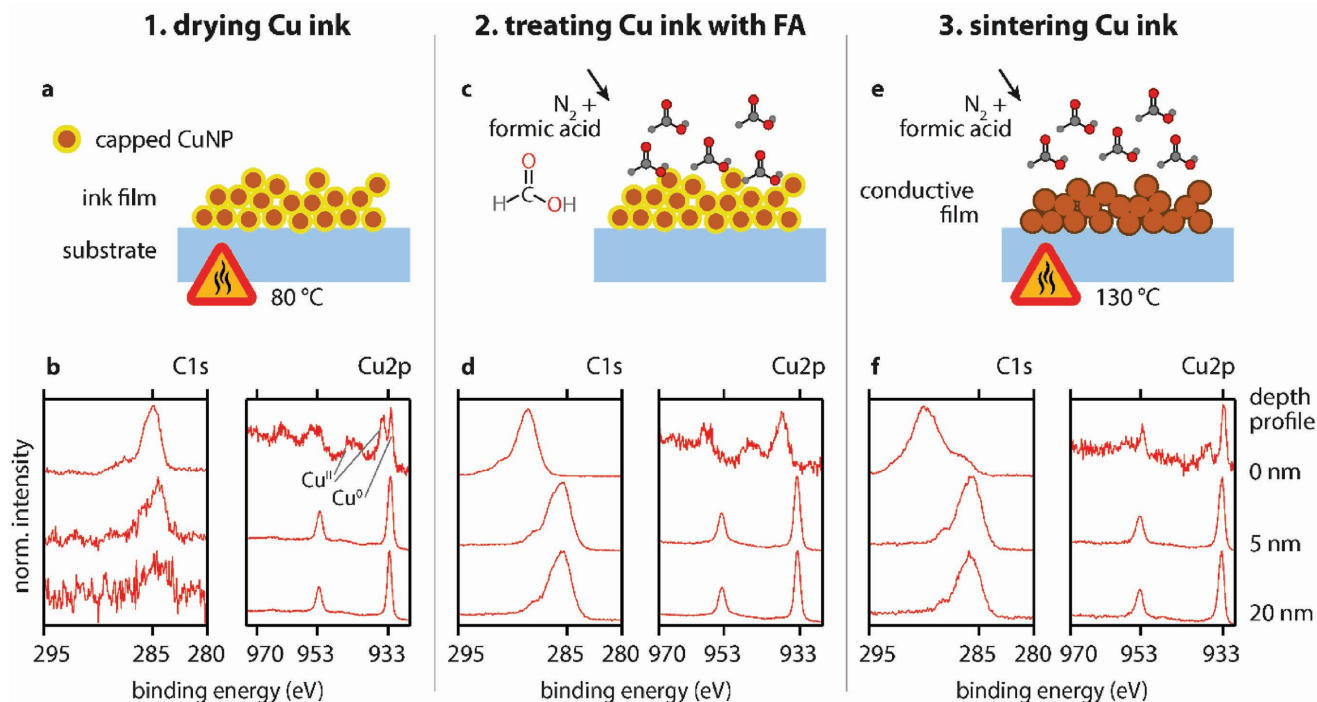


Figure 12. a) The dried nanoparticle film is subjected to c) formic acid (FA) treatment. Upon the influence of temperature in e) the sintering step the nanoparticles merge and form a sintered film. b,d,f) The developments of the C1s as well as Cu(II) and Cu(0) components of the Cu2p peak are visible in the normalized XPS spectra and corresponding depth profiles. Reproduced with permission.^[110] Copyright 2018, Wiley VCH.

In the next step of the treatment process, the sample films fill with formic acid after exposure to formic acid vapor at room temperature. In this step, the protective ligand used on the nanoparticles is replaced by formates, as Cu surfaces show chemisorption of formic acid at room temperature.^[111] The process continues into the bulk film, resulting in a swelling and increase in film thickness. This is confirmed by the C1s signal in the depth profile XPS analysis, which displays (Figure 12, left panel, topmost spectra) the typical signals of the ligand also at the layers 5 and 20 nm below the surface. The film is still non-conductive at this stage, however, confirmed by the XPS signals of this bare substrate as the spectra show a shift of the peaks towards higher binding energy as a consequence of charging effects.^[112]

Upon the final sintering step (see schematic Figure 12), under application of the desired temperature and still in the presence of formic acid, desorption of the formates as well as evaporation of the solvent occurs, resulting in an overall reduction of organic compounds in the final films. As a consequence, the corresponding C1s peak in the depth profile XPS decreases (seen by the worsening signal-to-noise ratio, see Figure 12) and the Cu2p now shows a decreased Cu(II) component but increased ratio of Cu(0)—confirmed by the fact the film is now conductive.

The final conductivity is a function of temperature, which can be attributed to the increased formate desorption and solvent evaporation from the CuNPs. The presence of formic acid is mandatory to avoid Cu oxidation and achieve conductive films. Crucially for the low temperature-compatible sintering, two processes begin to occur from 130 °C onward: First,

formate decomposition and reduction of the surface Cu takes place on the Cu NP surfaces.^[111,113] Second, the reduced CuNPs then initiate the sintering process and form conductive films, yielding an abrupt increase in conductivity noticeable at 130 °C.

When carrying out the final sintering step at 150 °C, 26% of bulk Cu conductivity was achieved on PET; with 25% bulk Cu conductivity achieved on the comparison glass substrate. At even higher temperatures the solvent evaporation and formate desorption are even more efficient, which is apparent following sintering at 230 °C on glass, whereby the high bulk Cu conductivity of 31% was reached.^[110]

5. Outlook

In the previous sections, the progress of implementing an overcoated Ag and embedded Ag grid conducting electrode has been elucidated. Then the progress of developing a Cu grid that has been implemented in optoelectronic devices and is compatible with low temperature sintering procedures was introduced. In this final section, an additional effect that plays a part in the transparent conducting electrode configuration of OLEDs in particular will be examined: the outcoupling of light. Optical out-coupling is an important factor of the external quantum efficiency (η_{ext}) of an OLED, as it is equal to internal quantum efficiency (η_{int}) multiplied by the fraction of out-coupled light (η_{c}).^[114]

When remembering the device performance discussed above in the findings of Kinner et al.,^[49] it is first of all necessary to compare the device performance of the produced OLEDs

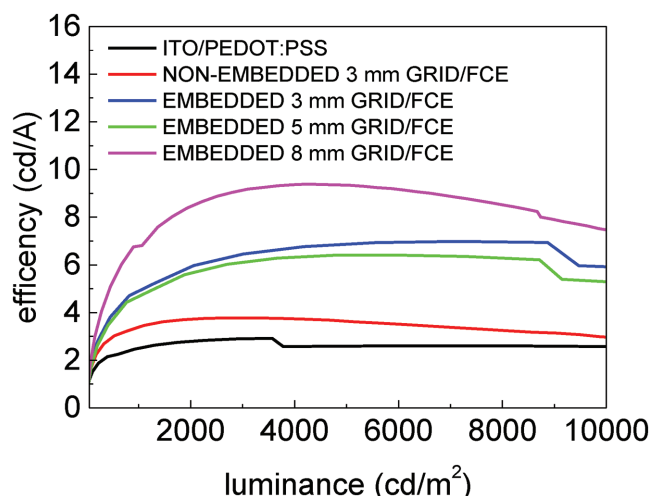


Figure 13. Current efficiency is vastly improved when moving from the ITO-based to non-embedded and then embedded grid architecture. Reproduced with permission.^[49] Copyright 2017, American Institute of Physics.

containing the ITO-based reference, 3 mm non-embedded and 3, 5, 8 mm embedded grid/PEDOT:PSS electrodes by considering the device efficiency as a function of the luminance (see Figure 13).

The OLED based on ITO has the lowest overall maximum device efficiency with 3.4 cd A^{-1} . Using the non-embedded 3 mm grid/PEDOT:PSS electrode, the OLED efficiency increases to a maximum of 3.7 cd A^{-1} below a luminance of $10\,000 \text{ cd m}^{-2}$. At the same time, the current density remains similar, in other words, more light is able to escape the device resulting in a higher current efficiency. At a higher current density of 6500 A m^{-2} , the ITO-based device shows a higher luminance of $13\,000 \text{ cd m}^{-2}$ versus the $12\,000 \text{ cd m}^{-2}$ for the non-embedded grid-based device (Figure 10).

This can be explained by an improved light out-coupling through the interface of PEDOT:PSS/glass compared to the interface of PEDOT:PSS/ITO/glass,^[115–117] especially at lower luminance. As the photons generated within the active layer of the ITO-based OLEDs encounter each interface on their way out of the device, 60–80% of this light is trapped because of the worse refractive index matching of the layer of ITO ($n = 2.10$ at 450 nm) in between the organic materials ($n \approx 1.75$) and glass ($n = 1.45$).^[118]

Using the transfer matrix method, light outcoupling was calculated for normal incident light at 450 nm , without inclusion of the identical Ca/Al top contact. Applying the method yielded a transmittance of 80% for the ITO-based device stack, while the non-embedded grid-based device had a transmittance of 99% (grid lines are not accounted for). It is reasonable to assume both devices have a similar η_{int} due to the identical cathode layer mentioned above, as well as the same light-emitting layer and operation at comparable current densities. An improved efficiency (η_{ext}) (shadowing and electrical losses are not accounted for) of 22% for light outcoupling.

Moving to embedding, the OLEDs built on the 3 and 5 mm embedded grid/PEDOT:PSS electrodes yield device efficiencies of up to 7 and 6.4 cd A^{-1} , respectively. This efficiency increase

when moving from non-embedding to embedding is not only due to the improvement in reduction of the leakage currents. Since the OLEDs incorporating the embedded 3 mm grid show a significantly higher luminance of $40\,000 \text{ cd m}^{-2}$ at 6500 A m^{-2} than the $12\,000 \text{ cd m}^{-2}$ of the non-embedded 3 mm grid device, this indicates a further improvement in light outcoupling from the device.

This is due to the improved refractive index matching when the layer of ITO ($n = 2.10$) is replaced with the resin Ormo-comp ($n = 1.52$), into which the grids are embedded, thereby allowing more light to be extracted from the device.^[119] (It must be noted that in some parts of the grid the light is completely blocked from escaping due to the presence of the grid line itself, so that this is an average effect across the whole transparent anode). Finally, OLEDs incorporating the 8 mm grid/PEDOT:PSS electrode exhibit the highest efficiency of all investigated devices of up to 9.4 cd A^{-1} . The grid geometry has been improved by minimizing the remaining grid lines across the active area and as a result any remaining shunt losses are reduced, while also significantly reducing light blocking.

The explanation for this final improvement in device efficiency needs to take into account the light that couples into the substrate as well as into waveguide modes. Typically, the percentage of the light generated within the OLED, which couples into the combination of waveguide, substrate, plasmonic as well as other electrical loss modes is within the same order of magnitude or higher than the percentage of outcoupled light.^[120–122] This means that if light is not lost into these loss channels and due to the calculated out-coupling factor $\eta_c(\lambda)$ being close to 99%, light otherwise lost into waveguide and substrate modes will be coupled out of the device and yield the observed overall increase in device efficiency.^[49]

Besides these outcoupling considerations, the printing of nanoparticle grids can be combined with imprinting methods to access plasmonic effects. For example, plasmonic nanoparticle arrays that feature collective lattice resonances (CLRs), i.e., plasmon resonance-induced grating effects,^[123,124] can allow a high level of control over light outcoupling.

By employing Al nanoparticle arrays embedded within the color conversion layer of solid-state lighting devices, light emission has been improved as a result of enhanced light generation and outcoupling.^[125] More recently, CLRs showed enhancement within light-emitting field effect transistors^[126] and such arrays can also serve to tune the emission color of an OLED. This is achieved by balancing the ohmic damping of the localized surface plasmon resonance and the CLRs through the choice of the lattice constant.^[127]

By selecting the appropriate lattice constant of an Al nanodisc array with square shaped symmetry and embedding it within a phosphorescent blue OLED configuration, device performance is improved by increasing the current efficiency by 35%.^[128] At the same time, an imprinted grating can be used to enhance the absorption over a broad wavelength range.^[129]

It is clear that by combining printing with imprinting techniques such as nanoimprint lithography, plasmonic effects can be utilized to enhance light management, i.e., incoupling of light into an OPV and outcoupling of light from an OLED, to further enhance optoelectronic device performance.

By gaining ultimate control of all the improvements in incoupling and outcoupling of light for these types of optoelectronic devices, future applications can be envisioned that additionally take advantage of the material flexibility, which solution-processing provides. For example, wearable or stretchable electronics can be targeted by integrating OLEDs or OPVs into textiles, thereby advancing the wearable electronics industry.

6. Conclusions

This progress report has highlighted the implementation of printed nanoparticle-based ITO-free transparent conductive electrode in a series of optoelectronic devices. Starting from optimizing the Ag nanoparticle based bottom electrode properties of thickness and height and being able to apply a simple overcoat procedure to yield comparable performance to ITO-based OLED devices, the Ag-grid architecture was embedded to yield highly efficient OLED structures with superior device performance to those based on ITO.

Moving to printed Cu nanoparticles instead of Ag in order to address financial and resource-based considerations, the device efficiency in OPVs was shown to be slightly lower than those based on ITO, however, the devices were fully produced in ambient air conditions. Furthermore, by optimizing the sintering procedure required to produce conducting metal structures based on Cu metal nanoparticle inks, and by addressing its compatibility with low-temperature stable substrates, highly conductive Cu films could be produced, which will pave the way for implementation in fully functioning printed optoelectronic devices.

Finally, the important factor of light outcoupling was addressed in OLEDs by first utilizing the refractive index of the chosen resin in which the transparent conductive electrode is embedded to influence the outcoupling efficiency of light produced within the active layer. Second, by combining printing of nanoparticles with lithographically imprinted structures, plasmonic effects can be utilized to selectively enhance absorption as well as electroluminescence. All these approaches show the importance of continuing work in the printed conductive electrode for use in organic and hybrid optoelectronic devices in order to further improve device performance.

Acknowledgements

The authors gratefully acknowledge funding from the PLASMAS project through the European Union (FP7 Project No. 604568) as well as Helmholtz-Zentrum Berlin/HySprint. This work was carried out in the framework of the Joint Lab GEN_FAB. The authors thank the numerous collaborators and co-authors of the work described in the text for joint activities and fruitful discussions—in particular Dr. Christine Boeffel, Dr. Alexander Lange, Dr. Efthymios Georgiou, Dr. Marios Neophytou, Sergey Pozov, Dr. Achilleas Savva, Dr. Manuel Auer-Berger, Lukas Kinner, Dr. Andreas Klug, Dr. Sebastian Nau, Dr. Karl Popovic, Dr. Stefan Sax, Dr. Gerburg Schider, Dr. Ignasi Burgués-Ceballos, Dr. Richard Ward, David Burmeister, Dr. Giovanni Ligorio as well as Prof. Norbert Koch and Prof. Klaus Müllen. Dr. Ignasi Burgués-Ceballos and all other copyright holders are also gratefully acknowledged for granting permission for the use of Figures.

Conflict of Interest

The authors declare no conflict of interest.

Keywords

embedded silver and copper grid, inkjet-printed electronics, metal nanoparticle ink, solution-processed optoelectronics, transparent electrode

Received: September 25, 2018

Revised: November 13, 2018

Published online: January 3, 2019

- [1] J. H. Burroughes, D. D. C. Bradley, A. R. Brown, R. N. Marks, K. MacKay, R. H. Friend, P. L. Burns, A. B. Holmes, *Nature* **1990**, 347, 539.
- [2] R. H. Friend, R. W. Gymer, A. B. Holmes, J. H. Burroughes, R. N. Marks, C. Taliani, D. D. C. Bradley, D. A. dos Santos, J. L. Brédas, M. Lögdlund, W. R. Salaneck, *Nature* **1999**, 397, 121.
- [3] T. Sekitani, H. Nakajima, H. Maeda, T. Fukushima, T. Aida, K. Hata, T. Someya, *Nat. Mater.* **2009**, 8, 494.
- [4] T. Sekitani, T. Someya, *Adv. Mater.* **2010**, 22, 2228.
- [5] J. A. Rogers, T. Someya, Y. Huang, *Science* **2010**, 327, 1603.
- [6] J. Liang, L. Li, X. Niu, Z. Yu, Q. Pei, *Nat. Photonics* **2013**, 7, 817.
- [7] S. Jung, S. Lee, M. Song, D.-G. Kim, D. S. You, J.-K. Kim, C. S. Kim, T.-M. Kim, K.-H. Kim, J.-J. Kim, J.-W. Kang, *Adv. Energy Mater.* **2014**, 4, 1300474.
- [8] M. A. Green, Y. Hishikawa, E. D. Dunlop, D. H. Levi, J. Hohl-Ebinger, A. W. Y. Ho-Baillie, *Prog. Photovoltaics* **2018**, 26, 427.
- [9] E. L. Unger, *Curr. Opin. Green Sustainable Chem.* **2017**, 4, 72.
- [10] E. L. Unger, L. Kegelmann, K. Suchan, D. Sörell, L. Korte, S. Albrecht, *J. Mater. Chem. A* **2017**, 5, 11401.
- [11] H. J. Snaith, *Nat. Mater.* **2018**, 17, 372.
- [12] S. Albrecht, M. Saliba, J. P. Correa Baena, F. Lang, L. Kegelmann, M. Mews, L. Steier, A. Abate, J. Rappich, L. Korte, R. Schlattmann, M. K. Nazeeruddin, A. Hagfeldt, M. Grätzel, B. Rech, *Energy Environ. Sci.* **2016**, 9, 81.
- [13] R. Abbel, P. Teunissen, E. Rubingh, T. van Lammeren, R. Cauchois, M. Everaars, J. Valetton, S. van de Geijn, P. Groen, *Transl. Mater. Res.* **2014**, 1, 015002.
- [14] R. Abbel, Y. Galagan, P. Groen, *Adv. Eng. Mater.* **2018**, 20, 1701190.
- [15] F. Hermerschmidt, I. Burgués-Ceballos, A. Savva, E. D. Sepos, A. Lange, C. Boeffel, S. Nau, E. J. W. List-Kratochvil, S. A. Choulis, *Flexible Printed Electron.* **2016**, 1, 035004.
- [16] M. Neophytou, F. Hermerschmidt, A. Savva, E. Georgiou, S. A. Choulis, *Appl. Phys. Lett.* **2012**, 101, 193302.
- [17] M. Neophytou, E. Georgiou, M. M. Fyrillas, S. A. Choulis, *Sol. Energy Mater. Sol. Cells* **2014**, 122, 1.
- [18] E. Georgiou, S. A. Choulis, F. Hermerschmidt, S. M. Pozov, I. Burgués-Ceballos, C. Christodoulou, G. Schider, S. Kreissl, R. Ward, E. J. W. List-Kratochvil, C. Boeffel, *Sol. RRL* **2018**, 2, 1700192.
- [19] H. Sirringhaus, T. Kawase, R. H. Friend, T. Shimoda, M. Inbasekaran, W. Wu, E. P. Woo, *Science* **2000**, 290, 2123.
- [20] S. Gamerith, A. Klug, H. Scheiber, U. Scherf, E. Moderegger, E. J. W. List, *Adv. Funct. Mater.* **2007**, 17, 3111.
- [21] M. Auer, L. Pevzner, S. Sax, E. J. W. List-Kratochvil, *Supramolecular Materials for Opto-Electronics*, Royal Society of Chemistry, Cambridge **2014**, p. 226.
- [22] N. Koch, *ChemPhysChem* **2007**, 8, 1438.
- [23] W. Brütting, S. Berleb, A. G. Mückl, *Org. Electron.* **2001**, 2, 1.

- [24] *Organic Light Emitting Devices* (Eds: K. Müllen, U. Scherf), Wiley, Weinheim, Germany **2005**.
- [25] A. van Dijken, A. Perro, E. A. Meulenkaamp, K. Brunner, *Org. Electron.* **2003**, 4, 131.
- [26] S. A. Choulis, V. E. Choong, A. Patwardhan, M. K. Mathai, F. So, *Adv. Funct. Mater.* **2006**, 16, 1075.
- [27] Y. Z. Wang, A. J. Epstein, *Acc. Chem. Res.* **1999**, 32, 217.
- [28] M. A. Green, *Solar Cells: Operating Principles, Technology and System Applications*, Prentice-Hall, Englewood Cliffs, NJ **1982**.
- [29] B. A. Gregg, *J. Phys. Chem. B* **2003**, 107, 4688.
- [30] G. D. Scholes, G. Rumbles, *Nat. Mater.* **2006**, 5, 683.
- [31] P. W. M. Blom, V. D. Mihailetschi, L. J. A. Koster, D. E. Markov, *Adv. Mater.* **2007**, 19, 1551.
- [32] J. Bredas, J. Cornil, A. J. Heeger, *Adv. Mater.* **1996**, 8, 447.
- [33] V. I. Arkhipov, H. Bässler, *Phys. Status Solidi A* **2004**, 201, 1152.
- [34] J.-L. Brédas, A. E. Norton, J. Cornil, V. Coropceanu, *Acc. Chem. Res.* **2009**, 42, 1691.
- [35] C. Deibel, T. Strobel, V. Dyakonov, *Adv. Mater.* **2010**, 22, 4097.
- [36] N. S. Sariciftci, L. Smilowitz, A. J. Heeger, F. Wudl, *Science* **1992**, 258, 1474.
- [37] A. Maurano, R. Hamilton, C. G. Shuttle, A. M. Ballantyne, J. Nelson, B. O'Regan, W. Zhang, I. McCulloch, H. Azimi, M. Morana, C. J. Brabec, J. R. Durrant, *Adv. Mater.* **2010**, 22, 4987.
- [38] W. Cao, J. Li, H. Chen, J. Xue, *J. Photonics Energy* **2014**, 4, 040990.
- [39] S. Ma, W. Qiao, T. Cheng, B. Zhang, J. Yao, A. Alsaedi, T. Hayat, Y. Ding, Z. A. Tan, S. Dai, *ACS Appl. Mater. Interfaces* **2018**, 10, 3902.
- [40] Z. Liu, T. He, H. Wang, X. Song, H. Liu, J. Yang, K. Liu, H. Ma, *RSC Adv.* **2017**, 7, 18456.
- [41] S. Nau, N. Schulte, S. Winkler, J. Frisch, A. Vollmer, N. Koch, S. Sax, E. J. W. List, *Adv. Mater.* **2013**, 25, 4420.
- [42] R. Trättnig, L. Pevzner, M. Jäger, R. Schlesinger, M. V. Nardi, G. Ligorio, C. Christodoulou, N. Koch, M. Baumgarten, K. Müllen, E. J. W. List, *Adv. Funct. Mater.* **2013**, 23, 4897.
- [43] M. Auer-Berger, R. Trättnig, T. Qin, R. Schlesinger, M. V. Nardi, G. Ligorio, C. Christodoulou, N. Koch, M. Baumgarten, K. M. Ilen, E. J. W. List-Kratochvil, *Org. Electron.* **2016**, 35, 164.
- [44] J. X. Zhou, J. Y. H. Fuh, H. T. Loh, Y. S. Wong, Y. S. Ng, J. J. Gray, S. J. Chua, *Int. J. Adv. Manuf. Technol.* **2010**, 48, 243.
- [45] F. C. Krebs, T. Tromholt, M. Jørgensen, *Nanoscale* **2010**, 2, 873.
- [46] I. Burgués-Ceballos, M. Stella, P. Lacharmoise, E. Martínez-Ferrero, *J. Mater. Chem. A* **2014**, 2, 17711.
- [47] Y. Galagan, B. Zimmermann, E. W. C. Coenen, M. Jørgensen, D. M. Tanenbaum, F. C. Krebs, H. H. Gortler, S. Sabik, L. H. Slooff, S. C. Veenstra, J. M. Kroon, R. Andriessen, *Adv. Energy Mater.* **2012**, 2, 103.
- [48] Y. Galagan, E. W. C. Coenen, R. Abbel, T. J. van Lammeren, S. Sabik, M. Barink, E. R. Meinders, R. Andriessen, P. W. M. Blom, *Org. Electron.* **2013**, 14, 38.
- [49] L. Kinner, S. Nau, K. Popovic, S. Sax, I. Burgués-Ceballos, F. Hermerschmidt, A. Lange, C. Boeffel, S. A. Choulis, E. J. W. List-Kratochvil, *Appl. Phys. Lett.* **2017**, 110, 101107.
- [50] A. Klug, P. Patter, K. Popovic, A. Blümel, S. Sax, M. Lenz, O. Glushko, M. J. Cordill, E. J. W. List-Kratochvil, *Proc. SPIE* **2015**, 9569, 95690N.
- [51] E. Georgiou, A. Savva, M. Neophytou, F. Hermerschmidt, T. Demosthenous, S. A. Choulis, *Appl. Phys. Lett.* **2014**, 105, 233901.
- [52] F. Hermerschmidt, P. Papagiorgis, A. Savva, C. Christodoulou, G. Iktos, S. A. Choulis, *Sol. Energy Mater. Sol. Cells* **2014**, 130, 474.
- [53] S. Jung, A. Sou, K. Banger, D.-H. Ko, P. C. Y. Chow, C. R. McNeill, H. Sirringhaus, *Adv. Energy Mater.* **2014**, 4, 1400432.
- [54] T. M. Eggenhuisen, Y. Galagan, A. F. K. V. Biezemans, T. M. W. L. Slaats, W. P. Voorthuizen, S. Kommeren, S. Shanmugam, J. P. Teunissen, A. Hadipour, W. J. H. Verhees, S. C. Veenstra, M. J. J. Coenen, J. Gilot, R. Andriessen, W. A. Groen, *J. Mater. Chem. A* **2015**, 3, 7255.
- [55] J.-S. Yu, I. Kim, J.-S. Kim, J. Jo, T. T. Larsen-Olsen, R. R. Søndergaard, M. Hösel, D. Angmo, M. Jørgensen, F. C. Krebs, *Nanoscale* **2012**, 4, 6032.
- [56] C. N. Hoth, S. A. Choulis, P. Schilinsky, C. J. Brabec, *Adv. Mater.* **2007**, 19, 3973.
- [57] C. Peng, Z. Jia, H. Neilson, T. Li, J. Lou, *Adv. Eng. Mater.* **2013**, 15, 250.
- [58] K. Ellmer, *Nat. Photonics* **2012**, 6, 809.
- [59] J. D. Servaites, S. Yeganeh, T. J. Marks, M. A. Ratner, *Adv. Funct. Mater.* **2010**, 20, 97.
- [60] Y.-F. Liu, J. Feng, Y.-F. Zhang, H.-F. Cui, D. Yin, Y.-G. Bi, J.-F. Song, Q.-D. Chen, H.-B. Sun, *Org. Electron.* **2014**, 15, 478.
- [61] A. Fallahzadeh, J. Saghaei, M. H. Yousefi, *Appl. Surf. Sci.* **2014**, 320, 895.
- [62] Y. Li, X. Hu, S. Zhou, L. Yang, J. Yan, C. Sun, P. Chen, *J. Mater. Chem. C* **2014**, 2, 916.
- [63] T.-H. Han, Y. Lee, M.-R. Choi, S.-H. Woo, S.-H. Bae, B. H. Hong, J. H. Ahn, T.-W. Lee, *Nat. Photonics* **2012**, 6, 105.
- [64] Q.-Q. Zhuo, Q. Wang, Y.-P. Zhang, D. Zhang, Q.-L. Li, C.-H. Gao, Y.-Q. Sun, L. Ding, Q.-J. Sun, S.-D. Wang, J. Zhong, X.-H. Sun, S.-T. Lee, *ACS Nano* **2015**, 9, 594.
- [65] D. S. Hecht, L. Hu, G. Irvin, *Adv. Mater.* **2011**, 23, 1482.
- [66] W. Gaynor, S. Hofmann, M. G. Christoforo, C. Sachse, S. Mehra, A. Salleo, M. D. McGehee, M. C. Gather, B. Lüssem, L. Müller-Meskamp, P. Peumans, K. Leo, *Adv. Mater.* **2013**, 25, 4006.
- [67] C. Sachse, N. Weiß, N. Gaponik, L. Müller-Meskamp, A. Eychmüller, K. Leo, *Adv. Energy Mater.* **2014**, 4, 1300737.
- [68] W.-K. Kim, S. Lee, D. H. Lee, I. H. Park, J. S. Bae, T.-W. Lee, J.-Y. Kim, J. H. Park, Y. C. Cho, C. R. Cho, S.-Y. Jeong, *Sci. Rep.* **2015**, 5, 10715.
- [69] S. Choi, S.-J. Kim, C. Fuentes-Hernandez, B. Kippelen, *Opt. Express* **2011**, 19, A793.
- [70] T. Bockrocker, N. Hülsmann, C. Eschenbaum, A. Pargner, S. Höfle, F. Maier-Flaig, U. Lemmer, *Thin Solid Films* **2013**, 542, 306.
- [71] F. L. M. Sam, C. A. Mills, L. J. Rozanski, S. R. P. Silva, *Laser Photonics Rev.* **2014**, 8, 172.
- [72] M. Zhang, S. Höfle, J. Czolk, A. Mertens, A. Colmann, *Nanoscale* **2015**, 7, 20009.
- [73] Z. Shu, E. Beckert, R. Eberhardt, A. Tünnermann, *J. Mater. Chem. C* **2017**, 5, 11590.
- [74] T. Vidmar, M. Topič, P. Dzik, U. Opara Krašovec, *Sol. Energy Mater. Sol. Cells* **2014**, 125, 87.
- [75] I. Burgués-Ceballos, N. Kehagias, C. M. Sotomayor-Torres, M. Campoy-Quiles, P. D. Lacharmoise, *Sol. Energy Mater. Sol. Cells* **2014**, 127, 50.
- [76] F. L. M. Sam, M. A. Razali, K. D. G. I. Jayawardena, C. A. Mills, L. J. Rozanski, M. J. Beliatas, S. R. P. Silva, *Org. Electron.* **2014**, 15, 3492.
- [77] L. Zhou, H.-Y. Xiang, S. Shen, Y.-Q. Li, J.-D. Chen, H.-J. Xie, I. A. Goldthorpe, L.-S. Chen, S.-T. Lee, J.-X. Tang, *ACS Nano* **2014**, 8, 12796.
- [78] S. Choi, Y. Zhou, W. Haske, J. W. Shim, C. Fuentes-Hernandez, B. Kippelen, *Org. Electron.* **2015**, 17, 349.
- [79] H.-Y. Xiang, Y.-Q. Li, L. Zhou, H.-J. Xie, C. Li, Q.-D. Ou, L.-S. Chen, C.-S. Lee, S.-T. Lee, J.-X. Tang, *ACS Nano* **2015**, 9, 7553.
- [80] I. Burgués-Ceballos, *Doctoral Thesis*, Universitat Autònoma de Barcelona, Barcelona, **2014**.

- [81] A. Chekane, B. Benyoucef, J. P. Charles, R. Zerdoum, M. Trari, *Sol. Energy Mater. Sol. Cells* **2005**, *87*, 557.
- [82] C. N. Hoth, P. Schilinsky, S. A. Choulis, C. J. Brabec, *Nano Lett.* **2008**, *8*, 2806.
- [83] A. Kamyshny, S. Magdassi, *Small* **2014**, *10*, 3515.
- [84] J. Niittynen, E. Sowade, H. Kang, R. R. Baumann, M. Mäntysalo, *Sci. Rep.* **2015**, *5*, 452.
- [85] M. L. Allen, M. Aronniemi, T. Mattila, A. Alastalo, K. Ojanperä, M. Suhonen, H. Seppä, *Nanotechnology* **2008**, *19*, 175201.
- [86] M. Grouchko, A. Kamyshny, C. F. Mihailescu, D. F. Anghel, S. Magdassi, *ACS Nano* **2011**, *5*, 3354.
- [87] Y. Lee, J.-R. Choi, K. J. Lee, N. E. Stott, D. Kim, *Nanotechnology* **2008**, *19*, 415604.
- [88] J. Perelaer, B. J. de Gans, U. S. Schubert, *Adv. Mater.* **2006**, *18*, 2101.
- [89] F. M. Wolf, J. Perelaer, S. Stumpf, D. Bollen, F. Kriebel, U. S. Schubert, *J. Mater. Res.* **2013**, *28*, 1254.
- [90] C. Paquet, R. James, A. J. Kell, O. Mozenon, J. Ferrigno, S. Lafrenière, P. R. L. Malenfant, *Org. Electron.* **2014**, *15*, 1836.
- [91] C.-A. Lu, P. Lin, H.-C. Lin, S.-F. Wang, *Jpn. J. Appl. Phys.* **2007**, *46*, 4179.
- [92] S. Harkema, S. Mennema, M. Barink, H. Rooms, J. S. Wilson, T. van Mol, D. Bollen, *Proc. SPIE* **2009**, *7415*, 74150T.
- [93] Y. Galagan, E. W. C. Coenen, S. Sabik, H. H. Gorter, M. Barink, S. C. Veenstra, J. M. Kroon, R. Andriessen, P. W. M. Blom, *Sol. Energy Mater. Sol. Cells* **2012**, *104*, 32.
- [94] Y. Galagan, S. Shanmugam, J. P. Teunissen, T. M. Eggenhuisen, A. F. K. V. Biezemans, T. Van Gijseghem, W. A. Groen, R. Andriessen, *Sol. Energy Mater. Sol. Cells* **2014**, *130*, 163.
- [95] B. R. Patil, S. Shanmugam, J.-P. Teunissen, Y. Galagan, *Org. Electron.* **2015**, *21*, 40.
- [96] G. Polino, S. Shanmugam, G. J. P. Bex, R. Abbel, F. Brunetti, A. Di Carlo, R. Andriessen, Y. Galagan, *ACS Appl. Mater. Interfaces* **2016**, *8*, 2325.
- [97] J.-B. Bonekamp, A. J. Moulé, K. Meerholz, *Proc. SPIE* **2005**, *5937*, 593713.
- [98] W.-D. Yang, C.-Y. Liu, Z.-Y. Zhang, Y. Liu, S.-D. Nie, *RSC Adv.* **2014**, *4*, 60144.
- [99] D. C. Giancoli, *Physics for Scientists & Engineers with Modern Physics*, Pearson Prentice Hall, Upper Saddle River, NJ **2009**.
- [100] D. J. Griffiths, *Introduction to Electrodynamics*, Prentice Hall, Upper Saddle River, NJ **1999**.
- [101] I. Kim, J. Kim, *J. Appl. Phys.* **2010**, *108*, 102807.
- [102] I. Kim, Y. Kim, K. Woo, E.-H. Ryu, K.-Y. Yon, G. Cao, J. Moon, *RSC Adv.* **2013**, *3*, 15169.
- [103] K. Kim, S. Il Ahn, K. C. Choi, *Curr. Appl. Phys.* **2013**, *13*, 1870.
- [104] Y. S. Rosen, A. Yakushenko, A. Offenhäusser, S. Magdassi, *ACS Omega* **2017**, *2*, 573.
- [105] Y. Farraj, M. Grouchko, S. Magdassi, *Chem. Commun.* **2015**, *51*, 1587.
- [106] Infineon Technologies AG, (United States Patent Office) *Patent US 2015/0214095 A1*, **2015**.
- [107] Samsung Electro-Mechanics Co Ltd (United States Patent Office) *Patent US 8206609 B2*, **2012**.
- [108] T. Stubhan, I. Litzov, N. Li, M. Salinas, M. Steidl, G. Sauer, K. Forberich, G. J. Matt, M. Halik, C. J. Brabec, *J. Mater. Chem. A* **2013**, *1*, 6004.
- [109] A. Savva, E. Georgiou, G. Papazoglou, A. Z. Chrusou, K. Kapnisis, S. A. Choulis, *Sol. Energy Mater. Sol. Cells* **2015**, *132*, 507.
- [110] F. Hermerschmidt, D. Burmeister, G. Ligorio, S. M. Pozov, R. Ward, S. A. Choulis, E. J. W. List-Kratochvil, *Adv. Mater. Technol.* **2018**, *3*, 1800146.
- [111] M. Bowker, E. Rowbotham, F. M. Leible, S. Haq, *Surf. Sci.* **1996**, *349*, 97.
- [112] S. Hüfner, *Photoelectron Spectroscopy*, Springer, Berlin **2003**.
- [113] R. W. Joyner, M. W. Roberts, *Proc. R. Soc. A* **1976**, *350*, 107.
- [114] S. R. Forrest, D. D. C. Bradley, M. E. Thompson, *Adv. Mater.* **2003**, *15*, 1043.
- [115] Y. H. Kim, J. Lee, W. M. Kim, C. Fuchs, S. Hofmann, H.-W. Chang, M. C. Gather, L. Müller-Meskamp, K. Leo, *Adv. Funct. Mater.* **2014**, *24*, 2553.
- [116] Y. H. Kim, J. Lee, S. Hofmann, M. C. Gather, L. Müller-Meskamp, K. Leo, *Adv. Funct. Mater.* **2013**, *23*, 3763.
- [117] C. Wu, Y. Huang, C. Chen, W. Lee, W. Tsai, C. Lu, M. Jiao, C. Lin, in *Proc. Light, Energy and the Environment*, Suzhou, China **2015**, DTu2D.1.
- [118] Y. Sun, S. R. Forrest, *Nat. Photonics* **2008**, *2*, 483.
- [119] T. Tsutsui, M. Yahiro, H. Yokogawa, K. Kawano, M. Yokoyama, *Adv. Mater.* **2001**, *13*, 1149.
- [120] R. Meerheim, M. Furno, S. Hofmann, B. Lüssem, K. Leo, *Appl. Phys. Lett.* **2010**, *97*, 253305.
- [121] S. Nowy, B. C. Krummacker, J. Frischeisen, N. A. Reinke, W. Brütting, *J. Appl. Phys.* **2008**, *104*, 123109.
- [122] S. Reineke, M. Thomschke, B. Lüssem, K. Leo, *Rev. Mod. Phys.* **2013**, *85*, 1245.
- [123] B. Auguie, W. L. Barnes, *Phys. Rev. Lett.* **2008**, *101*, 430.
- [124] S. Murai, M. A. Verschuuren, G. Lozano, G. Pirruccio, S. R. K. Rodriguez, J. G. Rivas, *Opt. Express* **2013**, *21*, 4250.
- [125] G. Lozano, D. J. Louwers, S. R. Rodriguez, S. Murai, O. T. Jansen, M. A. Verschuuren, J. Gómez Rivas, *Light: Sci. Appl.* **2013**, *2*, e66.
- [126] Y. Zakharko, M. Held, A. Graf, T. Rödlmeier, R. Eckstein, G. Hernandez-Sosa, B. Hähnlein, J. Pezoldt, J. Zaumseil, *ACS Photonics* **2016**, *3*, 2225.
- [127] M. Auer-Berger, V. Tretnak, F.-P. Wenzl, J. R. Krenn, *Opt. Eng.* **2017**, *56*, 1.
- [128] M. Auer-Berger, V. Tretnak, F.-P. Wenzl, J. R. Krenn, E. J. W. List-Kratochvil, *Appl. Phys. Lett.* **2017**, *111*, 173301.
- [129] I. Khan, H. Keshmiri, F. Kolb, T. Dimopoulos, E. J. W. List-Kratochvil, J. Dostalek, *Adv. Opt. Mater.* **2016**, *4*, 435.